Hydrogen susceptibility of an interstitial equimolar high-entropy alloy revealed by in-situ electrochemical microcantilever bending test

Xu Lu [a], Dong Wang [a], Zhiming Li [b, c], Yun Deng [a,*], Afrooz Barnoush [a]

[a] *Department of Mechanical and Industrial Engineering, Norwegian University of Science and Technology, No-7491 Trondheim, Norway*
[b] *Max-Planck-Institut für Eisenforschung, Max-Planck-Straße 1, D-40273, Düsseldorf, Germany*
[c] *School of Materials Science and Engineering, Central South University, Changsha 410083, China*

Abstract: Hydrogen effect on an interstitial CoCrFeMnNi high-entropy alloy was investigated by micro-cantilever bending tests with pre-notched {111} plane as a case study. Results showed sharp mode I cracks on (001) plane bisecting two {111} planes in hydrogen-charged cantilevers, which was explained by hydrogen-assisted defects formation and hydrogen pins dislocation motion.

1. Introduction

The development of high-entropy alloys (HEAs) opened a new era of alloying design with multi-principal elements in equimolar or near-equimolar ratios [1-4]. These alloys show excellent mechanical properties at various temperatures [5-8], which offer HEA with promising applications in transportation, nuclear construction, etc [9]. However, hydrogen effect on the mechanical properties of HEA is critical and should be studied in detail before applications. This is due to the fact that hydrogen is generally presented in the service environment of engineering materials. The Cantor alloy [2], i.e., equimolar CoCrFeMnNi with a single-phase face-centered cubic (FCC) structure was recently reported to exhibit good resistance to hydrogen embrittlement at a relatively low hydrogen content less than 4290.1 at. ppm (76.5 mass ppm) [10-13]. However, when the hydrogen content reaches to a level more than 6337.0 at. ppm (113.0 mass ppm), this HEA is also susceptible to hydrogen embrittlement [14, 15]. More recently, the interstitial carbon doped equiatomic and non-equiatomic HEAs were reported to possess higher tensile strength with enhanced work hardening behavior compared to carbon-free reference materials [10, 11, 14]. Also, the hydrogen embrittlement behavior of a typical interstitial HEA with nominal composition $Co_{19.9}Cr_{19.9}Fe_{19.9}Mn_{19.9}Ni_{19.9}C_{0.5}$ (at. %) was studied in a macroscale level [16]. This interstitial HEA showed a mixture of intergranular and transgranular fracture as well as microvoid coalescence in presence of 315.6 at. ppm (5.65 mass ppm) hydrogen, companied by a 12 % reduction in fracture elongation [16]. However, macroscale tests are not capable of providing an intuitive view of hydrogen-metal/defects interactions due to the unavoidable effects

of grain boundaries and complex stress/strain states in each grain. Thus, we used the recently developed micro-cantilever bending test in combination with in-situ hydrogen charging [17-21] to reveal the effect of hydrogen on the cracking behavior of a FCC structured interstitial HEA. By using a controllable hydrogen charging method, the local cracking behavior at stress concentrated areas was traced and compared explicitly in both hydrogen-free and hydrogen-charged environment.

2. Materials and experimental procedure

The homogenized interstitial equimolar CoCrFeMnNi HEA with nominal composition $Co_{19.9}Cr_{19.9}Fe_{19.9}Mn_{19.9i}Ni_{19.9}C_{0.5}$ (at. %) and an average grain size of 226 μm was used. The material was prepared by casting and hot-rolling at 900 °C, followed by homogenization at 1200 °C for 2 hours and water-quenching [22]. The samples were prepared by grinding and mechanical polishing, followed by electropolishing in a methanolic H_2SO_4 solution as the final step to obtain a deformation-free surface [23]. Both high-resolution scanning electron microscopy (SEM, Thermo Fisher Scientific Inc., USA.) and electron backscattered diffraction (EBSD) were used to define the directions for milling cantilevers, as shown in Fig. 1 (a)-(b). Milling of cantilevers with pentagonal cross section was carried out by using focused ion beam (Helios Nanolab Dual Beam FIB, Thermo Fisher Scientific Inc., USA). Due to the lack of available data for the crystal planes that are most fragile to cracking, all the cantilevers were pre-notched to study the plane of {111} with the lowest surface energy. Fig. 1 (c) and Table 1 show the details of beam dimensions. By integrating a miniaturized three-electrode electrochemical cell into Hysitron TI950 TriboIndenter [17, 18, 20], in-situ micromechanical test revealing the effect of hydrogen upon deformation can be conducted. To introduce sufficient hydrogen, cantilevers were firstly charged at -1400 $mV/_{Hg/HgSO4}$ for 40 h (refers to H1), then further charged at -1600 $mV/_{Hg/HgSO4}$ for 20 h (refers to H2) in the electrolyte consisted of glycerol-based borax with 0.002 mol/L $Na_2S_2O_3$ [24]. This electrolyte is able to preserve the surface integrity and provide precise details of deformation after bending. We used a conical tip with a nominal tip radius of 0.5 μm to perform the bending tests. The load function was designed by integrating partial-loading-unloading sequences after yielding at a loading rate of 2 nm/s. Afterwards, SEM was used to visualize the microstructure evolution. Also, FIB thinning perpendicular to the notch plane was performed, and secondary electron (SE) images during each thinning step were taken at the cracking area. When the beams were milled to a thickness of approximately 200 nm, a novel transmission EBSD (t-EBSD) was applied for high-resolution post-mortem microstructure analysis, and transmission electron microscopy (TEM, JEM-2100, JEOL, Inc.) technique was applied to characterize the deformation substructure after bending.
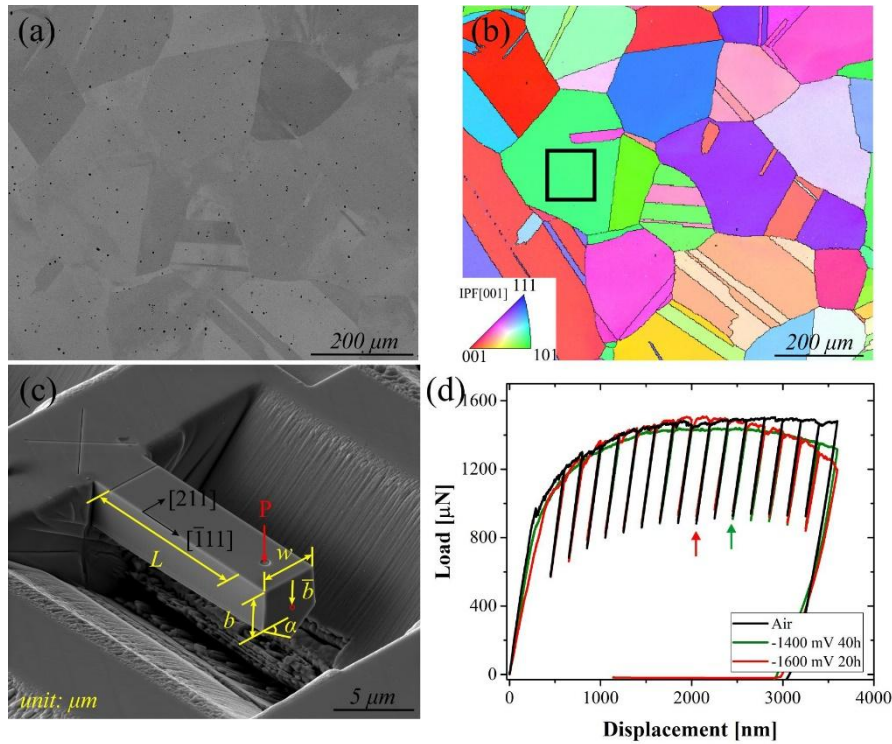
Fig. 1 (a) Back-scattered electron (BSE) micrograph of the studied interstitial HEA; (b) the corresponding inverse pole figure (IPF) map showing the selected grain orientation for milling cantilevers; (c) the characteristic dimensions of cantilevers; (d) load-displacement (L-D) curves of cantilevers bent in air and at two different hydrogen charging conditions, i.e., -1400 mV for 40 h (H1) and -1600 mV for 20 h (H2).

Table 1 Beam dimensions of cantilevers (dimensions in μm, angle in °). The symbols L, w, b, represent the length, width, side height of the beams. $\bar{b}$ is the distance from the upper surface to the geometric center, and α is the base angle of the isosceles triangle.

Beam	L	w	b	$\bar{b}$	α
Can_{air}	11.99±0.06	3.95±0.10	3.04±0.31	1.94±0.09	45
Can_H	11.99±0.02	4.00±0.05	2.86±0.04	1.89±0.04	45

3. Results and discussions

Fig. 1 (d) shows the representative load-displacement (L-D) curves obtained in air and at two charging conditions, i.e., H1 and H2. All beams exhibit linear elastic behavior in the first stage; the slight deviation in elastic properties could be caused by the small differentiation in beam geometries. Meanwhile, the absorption of hydrogen had no significant influence on yield strength (YS, defined as 0.2% offset stress). After reaching the yield points, L-D curves show similar plastic strain hardening regimes, and cantilever bent in air reaches plateau till unloading at 3500 nm displacement, while the flow stresses of beams tested in H1 and H2 conditions start decreasing gradually from the 11th and 9th of the loading-unloadign cycles, respectively, as marked by green and red arrows in Fig. 1 (d). The beam tested in H1 condition shows 8.4 %

reduction in the flow stress compared to the maximum stress value. By further decreasing the charging potential to -1600 mV (H2 condition), which approximates to an increment of current density by one order of magnitude, a reduction of 20.5 % in flow stress is observed.

Fig. 2 shows the micrographs of beams after bending at different conditions. To study the most noticeable effect of hydrogen, we chose H2 charging condition for the following discussion. In Fig. 2 (a1), abundant slip lines (marked by black lines) on the beam surface bent in air elucidate a large amount of plasticity was generated during deformation. According to Schmid's law, dislocation slips on (111), (11$\bar{1}$), and (1$\bar{1}$1) slip planes with an equal Schmid value of 0.272 were activated to compensate the plastic deformation, which is reflected by the slip traces on beam surface in Fig. 2 (a1). Here we use Schmid's law by assuming that on the top layer of the beams, uniaxial tensile stress dominated at the beginning of bending [25]. Notch blunting with a tip opening angle of 52.7° in air indicates a superior ductility and a high resistance to cracking of the studied interstitial HEA. The formation of microvoids at the crack tip, as pointed out by the white arrows in Fig. 2 (a1) and the magnified notch area in Fig. 2 (a2), elucidates a typical ductile fracture mode. On the contrary, beams bent in H2 condition had entirely different cracking behavior. Fig. 2 (b1) shows a sharp cracking of the notch plane (marked in red circle) with a smaller crack-tip opening angle of 27.2°. It is worth noting that the number of slip lines in Fig. 2 (b1) was remarkably reduced compared to that in Fig. 2 (a1), which indicates that the cracking process consumed part of the plasticity. And rugged fracture surfaces on the cracking plane shows a quasi-cleavage fracture behavior (Fig. 2 (b1)-(b2)). It is worth mentioning that due to the effect of beam size and the space limitation beneath the beams, it was unable to obtain fracture surfaces in the current tests. Optimization will be made in the following studies.
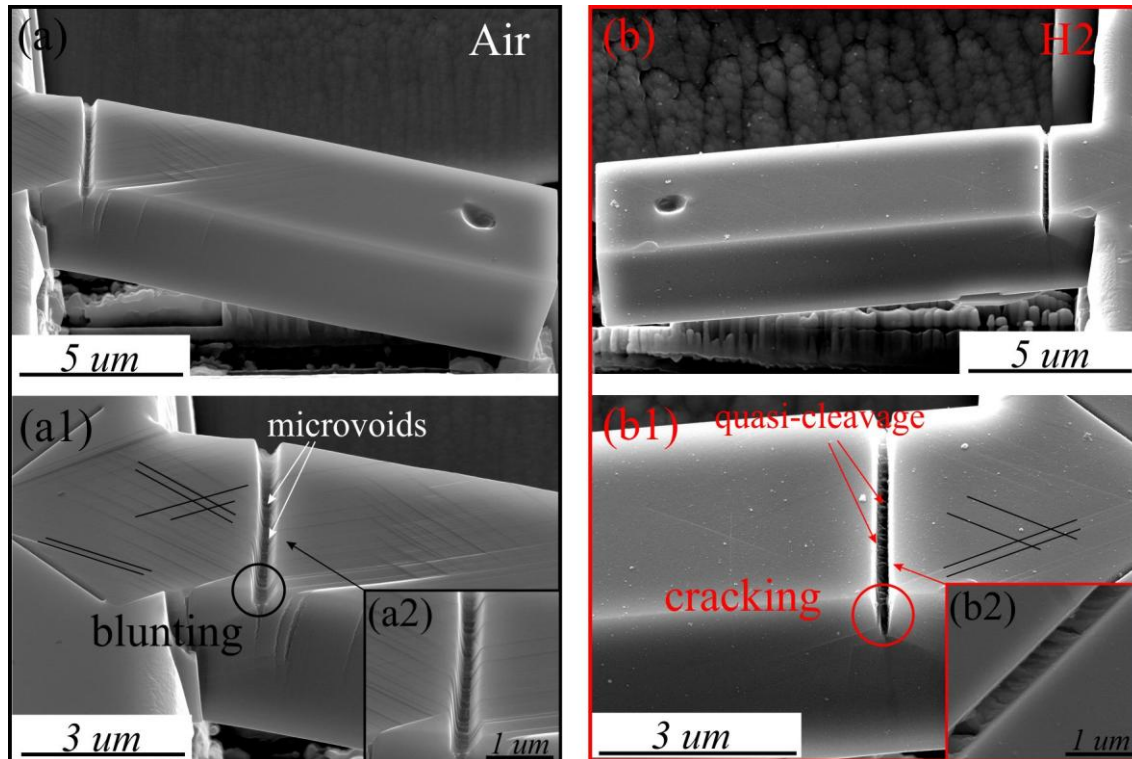
Fig. 2 (a), (a1) Secondary electron (SE) images showing deformation behavior of beams bent in air, and (b), (b1) in H2 charging condition; (a2) and (b2) magnified notch area in (a1) and (b1) after bending.

Fig. 3 shows the detailed characterization of beam cross sections after bending. Notch blunting is observed in the hydrogen-free condition (Fig. 3 (a1)-(a4)). At regions close to the beam surface, where plane stress condition prevails and plastic flow is relatively easy, the blunted notch shows a depth of 234.5 nm (Fig. 2 (a2)). This observation is consistent with the micrographs shown in Fig. 2 (a)-(a1). The notch crack becomes steep with an increase in depth of about 50 nm from beam surface (Fig. 3 (a2)) to the interior (Fig. 3 (a4)). In the central part of the beam, the notch tip sensed triaxial stress in a plane strain condition. And the more pronounced blunting behavior in the plane strain condition is caused by the difficulty of plastic flow and an enhanced stress concentration at the notch tip. Fig. 3 (a5) shows the Kernel Average Misorientation (KAM) map of the beam bent in air obtained from t-EBSD. Crystallographic misorientations beneath the notch tip indicates high geometrically necessary dislocation (GND) densities in three directions (marked with red dotted lines), which corresponds to the {111} slip traces marked in red. A large plastic zone is highlighted by the yellow dotted line. In comparison, hydrogen-assisted cracking happened on beams bent in H2 condition. In the plane stress condition, cracking propagated along the notch plane, followed by a deviation of the crack path into a non-specific-slip-plane (Fig. 3 (b2)). Fig. 3 (b3) shows the transition morphology of the crack from the surface to the middle region of the beam, i.e. cracking followed the notch plane for merely 80 nm then deviated as a sharp crack. In the plane strain condition, cracking deviated directly beneath the notch tip (Fig. 3 (b4)). Such variation in the cracking behavior on the beam surface and the center region is dependent on the local stress state. On the beam surface, the notch tip sensed less constraint from

the material, thus hydrogen-assisted cracking grew parallel to the notch plane. In comparison, the notch crack in the center region of the beam sensed a triaxial stress and cracking accordingly. KAM map in Fig. 3 (b5) shows a confined plastic zone compared to Fig. 3 (a5). Dislocation activities dominant in two slip planes, i.e., $(11\bar{1})$ and (111) (marked with red dotted lines). The resultant crack bisecting those two planes is aligned with (001) plane trace. Additionally, Fig. 3 (c) shows a reduced GND density in presence of hydrogen by measuring the crystallographic misorientations beneath the notch crack tip, which are highlighted by the yellow arrows in Fig. 3 (a5) and (b5). Further dislocation analyses on beam cross sections were performed with TEM. Bright-field images (Fig. 4 (a) and (b)) in two test conditions are consistent with the t-EBSD results. Deformation in air induced a large amount of plasticity below the blunted notch, and the high density of dislocations expand through the whole beam (Fig. 4 (a)). It is difficult to figure out dislocation structures since massive dislocations interact and tangle after deformation. Despite this, three slip bands can be clearly observed, which correspond to the active slip planes in Fig. 3 (a5). By contrast, hydrogen leads to a reduced and more localized plastic zone at the cracking area in Fig. 4 (b), which is consistent with the KAM map shown in Fig. 3 (b5). The two slip bands with high dislocation densities at the notch tip correspond to $(11\bar{1})$ and (111) plane traces, respectively.
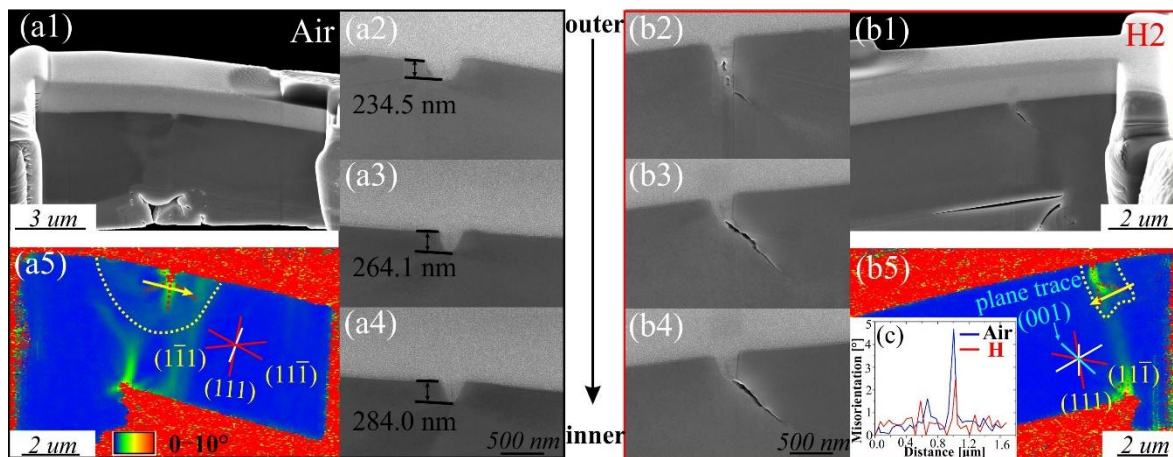

Fig. 3 SE images of beams cross-sections showing details of the cracking behavior (a1-a4) in air and (b1-b4) in H2 condition; (a5), (b5) KAM maps of two beams obtained from t-EBSD; and (c) misorientation data obtained close to the notch cracking.
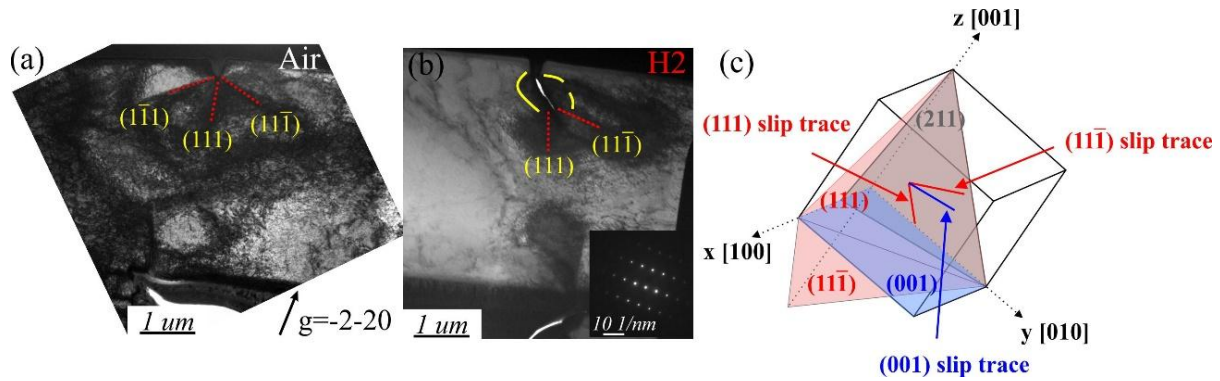
Fig. 4 Bright-field TEM micrographs showing dislocation morphologies of cantilevers bent in (a) air and (b) H2 condition; (c) a schematic showing the relation between the activated {111} slip planes and the (001) crack plane.

Based on the above results, the cracking behavior of the interstitial HEA is highly influenced by introducing hydrogen. In the hydrogen-free condition, when the plastic deformation began, the notch tip acted as a stress concentrator and dislocation nucleation started on the slip planes that reached the critical resolved shear stress. Dislocations generated at the notch tip continuously move away, which relieved the local stress effectively and the deformation process continued by notch blunting. All slip systems with the same Schmid factor were activated in the hydrogen-free beam to compensate the deformation process. As a result, a large plastic zone with a value of about 6.28 μm^2 was observed. In contrast, when hydrogen was presented at the notch tip, we observed a sharp crack with a reduced plastic zone (about 2.83 μm^2) instead of notch blunting. According to the "Defactant" model proposed by Kirchheim [26, 27], the formation energy of dislocations [24, 28] and vacancies was reduced by adding hydrogen. Dislocation nucleation and multiplication started upon plastic deformation. With hydrogen absorbed into the material and segregated to the dislocations, massive dislocation-dislocation and dislocation-hydrogen interactions were triggered at the notch tip. Also, the creation of strain-induced vacancies was enhanced by hydrogen atoms [29]. Hydrogen and hydrogen-vacancy clusters were proposed to effectively pin dislocations from movement [17, 19, 20, 30], as reflected by the reduced plastic zone at both sides of the crack. With further deformation, dislocations were unable to move away and local strain increased drastically due to pronounced dislocation interactions near the notch front. The local stress intensity gradually reached to the critical value for micro-cracks formation. As a result, the first micro-crack initiated, and the local deformation energy was released. The crack propagation was realized by operating multiple slips on alternating (11$\bar{1}$) and (111) planes, and a mode I crack on (001) plane was created bisecting two {111} planes. In this way, the plastic deformation was continuously consumed by the cracking process. Also, the nucleation and growth of microvoids at slip-band interactions or other defects ahead of the crack tip further contribute to the crack growth and result in a small crack-tip opening angle [31]. A schematic summary is shown in Fig. 4 (c), where cracking happened along $< 110 >$ direction on (001) plane. The projection of slip planes and crack plane on the beam cross-section is highlighted. The comparable resolved shear stress values for two intersecting conjugate {111} planes were proposed to cause the decohesion bisecting slip planes [32]. However, due to the complex stress state and dislocation activities at the notch tip, the values of resolved shear stress on each active

slip plane cannot be obtained in the current study. Therefore, further study will be performed by combining elastic-plastic fracture mechanics and discrete dislocation dynamics simulations to analyze the local stress values in each testing conditions.

4. Conclusions

In summary, hydrogen assisted cracking behavior of a carbon-doped equimolar CoCrFeMnNi high-entropy alloy (HEA) was studied by performing the in-situ micro-cantilever bending test in combination with advanced high-resolution characterizing techniques (transmission EBSD and TEM). Pre-notch on {111} plane was chosen as a case study. Results showed that this alloy exhibited superior strength and ductility upon loading in air, notch blunting alone was observed on the bent cantilevers. While in the hydrogen-charged cantilevers, a sharp cracking on (001) plane bisecting two {111} slip planes was observed. In this study, we show that the initiation and growth of micro-cracks were attributed to the synergetic effect of hydrogen-assisted defects formation and the pinning effect of hydrogen to dislocation motion, which causes the local stress intensity to reach to the critical value for micro-crack formation. As a result, a localized plasticity and a reduced average geometrically necessary dislocation (GND) density were observed. Worthy of mentioning, in order to understand the effect of grain orientation, different crack systems will be designed and tested to get a comprehensive view of hydrogen-assisted cracking in interstitial HEAs.

Data availability

The raw/processed data required to reproduce these findings cannot be shared at this time as the data also forms part of an ongoing study.

References

[1] J.W. Yeh, S.K. Chen, S.J. Lin, J.Y. Gan, T.S. Chin, T.T. Shun, C.H. Tsau, S.Y. Chang, Nanostructured high-entropy alloys with multiple principal elements: Novel alloy design concepts and outcomes, Adv. Eng. Mater. 6(5) (2004) 299-303.

[2] B. Cantor, I.T.H. Chang, P. Knight, A.J.B. Vincent, Microstructural development in equiatomic multicomponent alloys, Mater. Sci. Eng. A 375 (2004) 213-218.

[3] Z. Li, K.G. Pradeep, Y. Deng, D. Raabe, C.C. Tasan, Metastable high-entropy dual-phase alloys overcome the strength-ductility trade-off, Nature 534 (7606) (2016) 227-30.

[4] Y. Zhang, T.T. Zuo, Z. Tang, M.C. Gao, K.A. Dahmen, P.K. Liaw, Z.P. Lu, Microstructures and properties of high-entropy alloys, Prog. Mater. Sci. 61 (2014) 1-93.

[5] B. Gludovatz, A. Hohenwarter, D. Catoor, E.H. Chang, E.P. George, R.O. Ritchie, A fracture-resistant high-entropy alloy for cryogenic applications, Science 345(6201) (2014) 1153-1158.

[6] F. Otto, A. Dlouhy, C. Somsen, H. Bei, G. Eggeler, E.P. George, The influences of temperature and microstructure on the tensile properties of a CoCrFeMnNi high-entropy alloy, Acta Mater. 61(15) (2013) 5743-5755.

[7] Y.H. Jo, S. Jung, W.M. Choi, S.S. Sohn, H.S. Kim, B.J. Lee, N.J. Kim, S. Lee, Cryogenic strength improvement by utilizing room-temperature deformation twinning in a partially recrystallized VCrMnFeCoNi high-entropy alloy, Nat. Commun. 8 (2017).

[8] A.J. Zaddach, R.O. Scattergood, C.C. Koch, Tensile properties of low-stacking fault energy high-entropy alloys, Mater. Sci. Eng. A 636 (2015) 373-378.

[9] Y.F. Ye, Q. Wang, J. Lu, C.T. Liu, Y. Yang, High-entropy alloy: challenges and prospects, Mater. Today 19(6) (2016) 349-362.

[10] H. Luo, Z. Li, D. Raabe, Hydrogen enhances strength and ductility of an equiatomic high-entropy alloy, Sci. Rep. 7(1) (2017) 9892.

[11] Y. Zhao, D.-H. Lee, M.-Y. Seok, J.-A. Lee, M.P. Phaniraj, J.-Y. Suh, H.-Y. Ha, J.-Y. Kim, U. Ramamurty, J.-i. Jang, Resistance of CoCrFeMnNi high-entropy alloy to gaseous hydrogen embrittlement, Scr. Mater. 135 (2017) 54-58.

[12] H. Luo, Z.M. Li, A.M. Mingers, D. Raabe, Corrosion behavior of an equiatomic CoCrFeMnNi high-entropy alloy compared with 304 stainless steel in sulfuric acid solution, Corros. Sci. 134 (2018) 131-139.

[13] H. Luo, W. Lu, X. Fang, D. Ponge, Z. Li, D. Raabe, Beating hydrogen with its own weapon: Nano-twin gradients enhance embrittlement resistance of a high-entropy alloy, Mater. Today (2018).

[14] K.E. Nygren, K.M. Bertsch, S. Wang, H. Bei, A. Nagao, I.M. Robertson, Hydrogen embrittlement in compositionally complex FeNiCoCrMn FCC solid solution alloy, Curr.Opin. Solid St. M. (2017).

[15] K. Ichii, M. Koyama, C.C. Tasan, K. Tsuzaki, Comparative study of hydrogen embrittlement in stable and metastable high-entropy alloys, Scr. Mater. 150 (2018) 74-77.

[16] H. Luo, Z.M. Li, W.J. Lu, D. Ponge, D. Raabe, Hydrogen embrittlement of an interstitial equimolar high-entropy alloy, Corros. Sci. 136 (2018) 403-408.

[17] Y. Deng, A. Barnoush, Hydrogen embrittlement revealed via novel in situ fracture experiments using notched micro-cantilever specimens, Acta Mater. 142 (2018) 236-247.

[18] T. Hajilou, Y. Deng, B.R. Rogne, N. Kheradmand, A. Barnoush, In situ electrochemical microcantilever bending test: A new insight into hydrogen enhanced cracking, Scr. Mater. 132 (2017) 17-21.

[19] B.R.S. Rogne, N. Kheradmand, Y. Deng, A. Barnoush, In situ micromechanical testing in environmental scanning electron microscope: A new insight into hydrogen-assisted cracking, Acta Mater. 144 (2018) 257-268.

[20] Y. Deng, T. Hajilou, D. Wan, N. Kheradmand, A. Barnoush, In-situ micro-cantilever bending test in environmental scanning electron microscope: Real time observation of hydrogen enhanced cracking, Scr. Mater. 127 (2017) 19-23.

[21] Y. Deng, T. Hajilou, A. Barnoush, Hydrogen-enhanced cracking revealed by in situ micro-cantilever bending test inside environmental scanning electron microscope, Philos. Trans. Royal Soc. A 375(2098) (2017).

[22] Z. Li, Interstitial equiatomic CoCrFeMnNi high-entropy alloys: carbon content, microstructure, and compositional homogeneity effects on deformation behavior, Acta Mater. 164 (2019) 400-412.

[23] A. Barnoush, H. Vehoff, Electrochemical nanoindentation: A new approach to probe hydrogen/deformation interaction, Scr. Mater. 55(2) (2006) 195-198.

[24] D. Wang, X. Lu, Y. Deng, X. Guo, A. Barnoush, Effect of hydrogen on nanomechanical properties in Fe-22Mn-0.6C TWIP steel revealed by in-situ electrochemical nanoindentation, Acta Mater. 166 (2019) 618-629.

[25] B. Bhushan, Springer Handbook of Nanotechnology, 3 ed., Springer-Verlag Berlin Heidelberg2010.

[26] A. Pundt, R. Kirchheim, Hydrogen in metals: Microstructural aspects, Annu. Rev. Mater. Res. 36 (2006) 555-608.

[27] R. Kirchheim, Reducing grain boundary, dislocation line and vacancy formation energies by solute segregation. I. Theoretical background, Acta Mater. 55(15) (2007) 5129-5138.

[28] A. Barnoush, H. Vehoff, Recent developments in the study of hydrogen embrittlement: Hydrogen effect on dislocation nucleation, Acta Mater. 58(16) (2010) 5274-5285.

[29] K. Takai, H. Shoda, H. Suzuki, M. Nagumo, Lattice defects dominating hydrogen-related failure of metals, Acta Mater. 56(18) (2008) 5158-5167.

[30] D. Xie, S. Li, M. Li, Z. Wang, P. Gumbsch, J. Sun, E. Ma, J. Li, Z. Shan, Hydrogenated vacancies lock dislocations in aluminium, Nat. Commun. 7 (2016) 13341.

[31] S.P. Lynch, Mechanisms and Kinetics of Environmentally Assisted Cracking: Current Status, Issues, and Suggestions for Further Work, Metall. Mater. Trans. A 44a(3) (2013) 1209-1229.

[32] Q. Chen, H.W. Liu, Shear fatigue crack growth in large grain polycrystals, Proc. Am. Soc. Test. Mater. 1220 (1995) 467-483.

Hydrogen susceptibility of an interstitial equimolar high-entropy alloy revealed by in-situ electrochemical microcantilever bending test

Xu Lu [a], Dong Wang [a], Zhiming Li [b, c], Yun Deng [a,*], Afrooz Barnoush [a]

[a] *Department of Mechanical and Industrial Engineering, Norwegian University of Science and Technology, No-7491 Trondheim, Norway*
[b] *Max-Planck-Institut für Eisenforschung, Max-Planck-Straße 1, D-40273, Düsseldorf, Germany*
[c] *School of Materials Science and Engineering, Central South University, Changsha 410083, China*

Abstract: Hydrogen effect on an interstitial CoCrFeMnNi high-entropy alloy was investigated by micro-cantilever bending tests with pre-notched {111} plane as a case study. Results showed sharp mode I cracks on (001) plane bisecting two {111} planes in hydrogen-charged ~~samples~~cantilevers, which was explained by hydrogen-assisted defects formation and hydrogen pins dislocation motion.

Key words: Hydrogen embrittlement; micro-cantilever bending test; hydrogen enhanced localized plasticity; high-entropy alloy.

1. Introduction

The development of high-entropy alloys (HEAs) opened a new era of alloying design with multi-principal elements in equimolar or near-equimolar ratios [1-4]. These alloys show excellent mechanical properties at various temperatures [5-8], which ~~offers~~offer HEA with promising applications in transportation, nuclear construction, etc [9]. However, hydrogen effect on the mechanical properties of HEA is ~~the effect of hydrogen on HEA's mechanical properties are~~ critical and should be studied in detail before applications. This is due to the fact that hydrogen is generally presented in the service environment of engineering materials. The Cantor alloy [2], i.e., equimolar CoCrFeMnNi with a single-phase face-centered cubic (FCC) structure was recently reported to exhibit good resistance to hydrogen embrittlement at a relatively low hydrogen content less than 4290.1 at. ppm (76.5 mass ppm)~~(< 76.5 wt.ppm)~~ [10-13]. However, ~~hydrogen content environment (≥ 113 wt.ppm),~~ when the hydrogen content reaches to a level more than 6337.0 at. ppm (113.0 mass ppm), this HEA is also susceptible to hydrogen embrittlement~~HE~~ [14, 15]. More recently, the interstitial carbon doped equiatomic and non-equiatomic HEAs were reported to possess higher tensile strength with enhanced work hardening behavior compared to carbon-free reference materials [10, 11, 14]. Also, the hydrogen embrittlement behavior of a typical interstitial HEA with nominal composition $Co_{19.9}Cr_{19.9}Fe_{19.9}Mn_{19.9}Ni_{19.9}C_{0.5}$ (at. %) was studied in a macroscale level [16]. This interstitial HEA showed a mixture of intergranular and transgranular fracture as well as microvoid coalescence in presence of 315.6 at. ppm (5.65 mass ppm) hydrogen ~~(5.65 wt.ppm),~~ companied by a 12 % reduction in ~~tensile~~ fracture elongation [16].

However, macroscale tests are not capable of providing an intuitive view of hydrogen-metal/defects interactions due to the unavoidable effects of grain boundaries and complex stress/strain states in each grain. Thus, we used the recently developed micro-cantilever bending test in combination with in-situ hydrogen charging [17-21] to reveal the effect of hydrogen on the cracking behavior of a FCC structured interstitial HEA. By using a controllable hydrogen charging method, the local cracking behavior at stress concentrated areas was traced and compared explicitly in both hydrogen-free and hydrogen-charged environment.

2. Materials and experimental procedure

The homogenized interstitial equimolar CoCrFeMnNi HEA with nominal composition $Co_{19.9}Cr_{19.9}Fe_{19.9}Mn_{19.9i}Ni_{19.9}C_{0.5}$ (at. %) and an average grain size of 226 µm was used. The material was prepared by casting and hot-rolling at 900 °C, followed by homogenization at 1200 °C for 2 hours and water-quenching [22]. The samples were prepared by grinding and mechanical polishing, followed by electropolishing in a methanolic H_2SO_4 solution as the final step to obtain a deformation-free surface [23]. Both high-resolution scanning electron microscopy (SEM, Quanta FEG 650 ESEM, Thermo Fisher Scientific Inc., USA.) and electron backscattered diffraction (EBSD) were used to define the directions for milling cantilevers, as shown in Fig. 1 (a)-(b). Milling of cantilevers with pentagonal cross section was carried out by using focused-ion beam (Helios Nanolab Dual Beam FIB, Thermo Fisher Scientific Inc., USA). Due to the lack of available data for the crystal planes that are most fragile to cracking, all the cantilevers were pre-notched to study the plane of {111} with the lowest surface energy. Fig. 1 (c) and Table 1 show the details of beam dimensions. By integrating a miniaturized three-electrode electrochemical cell into Hysitron TI950 TriboIndenter [17, 18, 20], in-situ micromechanical test revealing the effect of hydrogen upon deformation can be conducted. To introduce sufficient hydrogen, cantilevers were first firstly charged at -1400 mV/$_{Hg/HgSO4}$ for 40 h (refers to H1), then further charged at -1600 mV/$_{Hg/HgSO4}$ for 20 h (refers to H2) in the electrolyte consisted of glycerol-based borax with 0.002 mol/L $Na_2S_2O_3$ [24]. This electrolyte is able to preserve the surface integrity and provide precise details of deformation after bending. We used a conical tip with a nominal tip radius of 0.5 µm to perform the bending tests. The load function was designed by integrating partial-loading-unloading sequences after yielding at a loading rate of 2 nm/s. Afterwards, SEM was used to visualize the microstructure evolution. Also, FIB thinning perpendicular to the notch plane was performed, and secondary electron (SE) images during each thinning step were taken at the cracking area. When the beams were milled to a thickness of approximately 200 nm, a novel transmission EBSD (t-EBSD) was applied for high-resolution post-mortem microstructure analysis, and transmission electron microscopy (TEM, JEM-2100, JEOL, Inc.) technique was applied to characterize the deformation substructure after bending.
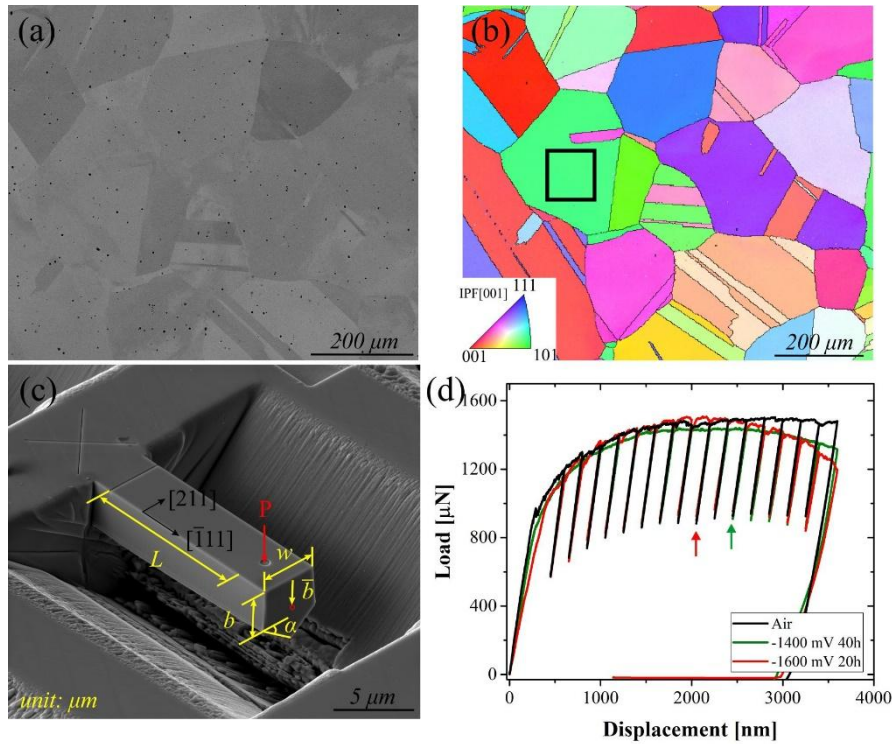
Fig. 1 (a) Back-scattered electron (BSE) micrograph of the studied interstitial HEA; (b) the corresponding inverse pole figure (IPF) map showing the selected grain orientation for milling cantilevers; (c) the characteristic dimensions of cantilevers; (d) load-displacement (L-D) curves of cantilevers bent in air and at two different hydrogen charging conditions, i.e., -1400 mV for 40 h (H1) and -1600 mV for 20 h (H2).

Table 1 Beam dimensions of cantilevers (dimensions in μm, angle in °). The symbols L, w, b, represent the length, width, side height of the beams. $\bar{b}$ is the distance from the upper surface to the geometric center, and α is the base angle of the isosceles triangle.

Beam	L	w	b	$\bar{b}$	α
Can_{air}	11.99±0.06	3.95±0.10	3.04±0.31	1.94±0.09	45
Can_H	11.99±0.02	4.00±0.05	2.86±0.04	1.89±0.04	45

3. Results and discussions

Fig. 1 (d) shows the representative load-displacement (L-D) curves obtained in air and at two charging conditions, i.e., H1 and H2. All beams exhibit linear elastic behavior in the first stage; the slight deviation in elastic properties could be caused by the small differentiation in beam geometries. Meanwhile, the absorption of hydrogen had no significant influence on yield strength (YS, defined as 0.2% offset stress). After reaching the yield points, L-D curves show similar plastic strain hardening regimes, and cantilever bent in air ~~reached~~ reaches plateau till unloading at 3500 nm displacement, while the flow stresses of beams tested in H1 and H2 conditions ~~started~~ start decreasing gradually from the ~~loading-unloading cycles 11 and 9~~ 11th and 9th of the loading-unloadign cycles, respectively, as marked by green and red arrows in Fig. 1 (d). The beam tested

in H1 condition shows~~showed~~ 8.4 % reduction in the flow stress compared to the maximum stress value. By further decreasing the charging potential to -1600 mV (H2 condition), which approximates to an increment of current density by one order of magnitude, a reduction of 20.5 % in flow stress ~~was~~ is observed.

Fig. 2 shows the micrographs of beams after bending at different conditions. To study the most noticeable effect of hydrogen, we chose H2 charging condition ~~in~~ for the following discussion. In Fig. 2 (a1), abundant slip lines (marked by black lines) on the beam surface bent in air ~~elucidating~~ elucidate a large amount of plasticity was generated during deformation. According to Schmid's law, dislocation slips on (111), (11$\bar{1}$), and (1$\bar{1}$1) slip planes with an equal Schmid value of 0.272 were activated to compensate the plastic deformation ~~with an equal Schmid value of 0.272~~, which is reflected by the slip traces on beam surface in Fig. 2 (a1). Here we use Schmid's law by assuming that on the top layer of the beams, uniaxial tensile stress dominated at the beginning of bending [25]. Notch blunting with a tip opening angle of 52.7° in ~~the~~ air indicates a superior ductility and a high resistance to cracking of the studied interstitial HEA. The formation of microvoids at the crack tip, as pointed out by the white arrows in Fig. 2 (a1) and the magnified notch area in Fig. 2 (a2), elucidates a typical ductile fracture mode. On the contrary, beams bent in H2 condition had entirely different cracking behavior. Fig. 2 (b1) shows a sharp cracking of the notch plane (marked in red circle) with a smaller crack-tip opening angle of 27.2°. It is worth noting that the number of slip lines in Fig. 2 (b1) was remarkably reduced compared to that in Fig. 2 (a1), which indicates that the cracking process consumed part of the plasticity. And rugged fracture surfaces on the cracking plane shows a quasi-cleavage fracture behavior (Fig. 2 (b1)-(b2)). It is worth mentioning that due to the effect of beam size and the space limitation beneath the beams, it was unable to obtain fracture surfaces in the current tests. Optimization will be made in the following studies.
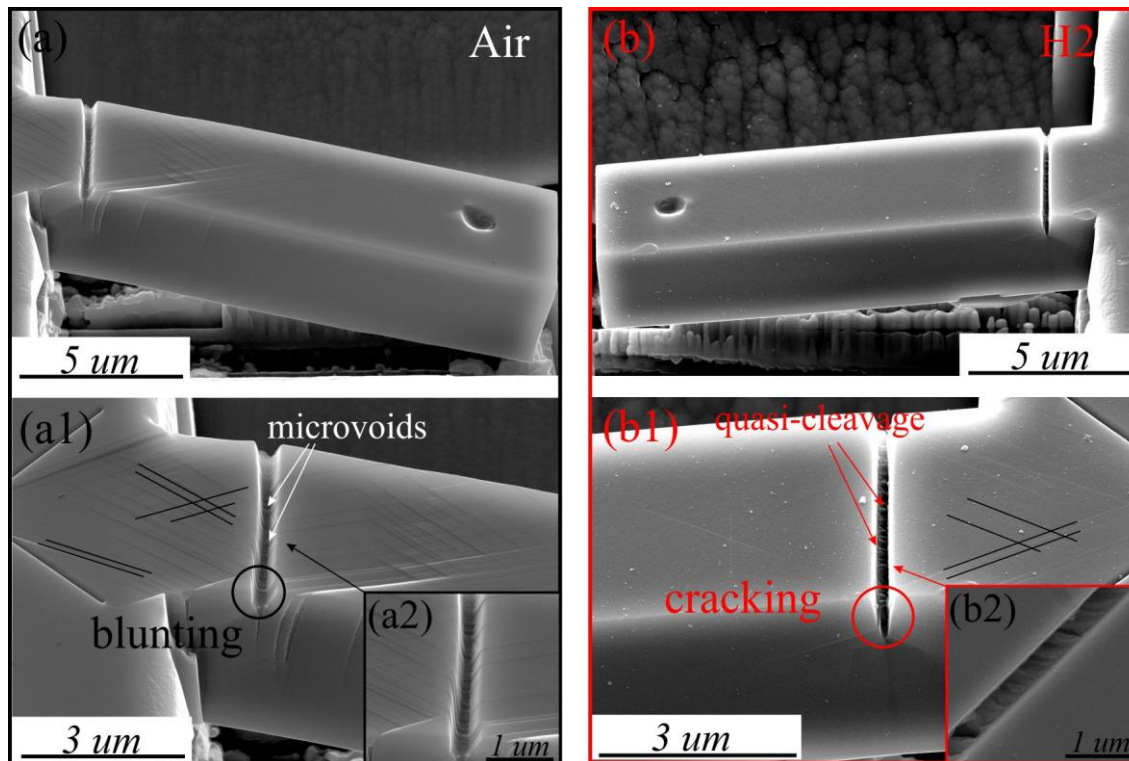
Fig. 2 (a), (a1) Secondary electron (SE) images showing deformation behavior of beams bent in air, and (b), (b1) in H2 charging condition; (a2) and (b2) magnified notch area in (a1) and (b1) after bending.

Fig. 3 shows the detailed characterization of beam cross sections after bending. Notch blunting ~~was~~ is observed in the hydrogen-free condition (Fig. 3 (a1)-(a4)). At regions close to the beam surface, where plane stress condition prevails and plastic flow is relatively easy, the blunted notch ~~showed~~ shows a depth of 234.5 nm (Fig. 2 (a2)). This observation is consistent with the micrographs shown in Fig. 2 (a)-(a1). The notch crack ~~became~~ becomes steep with an increase in depth of about 50 nm from beam surface (Fig. 3 (a2)) to the interior (Fig. 3 (a4)). In the central part of the beam, the notch tip sensed triaxial stress in a plane strain condition. And the more pronounced blunting behavior in the plane strain condition is caused by the difficulty of plastic flow and an enhanced stress concentration at the notch tip. Fig. 3 (a5) shows the Kernel Average Misorientation (KAM) map of the beam bent in air obtained from t-EBSD. Crystallographic misorientations beneath the notch tip ~~indicated~~ indicates high geometrically necessary dislocation (GND) densities in three directions (marked with red dotted lines), which corresponds to the {111} slip traces marked in red. A large plastic zone is highlighted by the yellow dotted line. In comparison, hydrogen-assisted cracking happened on beams bent in H2 condition. In the plane stress condition, cracking propagated along the notch plane, followed by a deviation of the crack path into a non-specific-slip-plane (Fig. 3 (b2)). Fig. 3 (b3) shows the transition morphology of the crack from the surface to the middle region of the beam, i.e. cracking followed the notch plane for merely 80 nm then deviated as a sharp crack. In the plane strain condition, cracking deviated directly beneath the notch tip (Fig. 3 (b4)). Such variation in the cracking behavior on the beam surface and the center region is dependent on the local stress state. On the beam surface,

the notch tip sensed less constraint from the material, thus hydrogen-assisted cracking grew parallel to the notch plane. In comparison, the notch crack in the center region of the beam sensed a triaxial stress and cracking accordingly. KAM map in Fig. 3 (b5) shows a confined plastic zone compared to Fig. 3 (a5). Dislocation activities dominant in two slip planes, i.e., $(11\bar{1})$ and (111) (marked with red dotted lines). The resultant crack bisecting those two planes is aligned with (001) plane trace. Additionally, Fig. 3 (c) shows a reduced GND density in presence of hydrogen by measuring the crystallographic misorientations beneath the notch crack tip, which are highlighted by the yellow arrows in Fig. 3 (a5) and (b5). Further dislocation analysis analyses on beam cross sections was were performed with TEM. Bright-field images (Fig. 4 (a) and (b)) in two test conditions are consistent with the t-EBSD results. Deformation in air induced a large amount of plasticity below the blunted notch, and the high density of dislocations expand through the whole beam (Fig. 4 (a)). It is difficult to figure out dislocation structures since massive dislocations interact and tangle after deformation. Despite this, three slip bands can be clearly observed, which corresponds correspond to the active slip planes in Fig. 3 (a5). By contrast, hydrogen leads to a reduced and more localized plastic zone at the cracking area in Fig. 4 (b), which is consistent with the KAM map shown in Fig. 3 (b5). The two slip bands with high dislocation densities at the notch tip correspond to $(11\bar{1})$ and (111) plane traces, respectively.
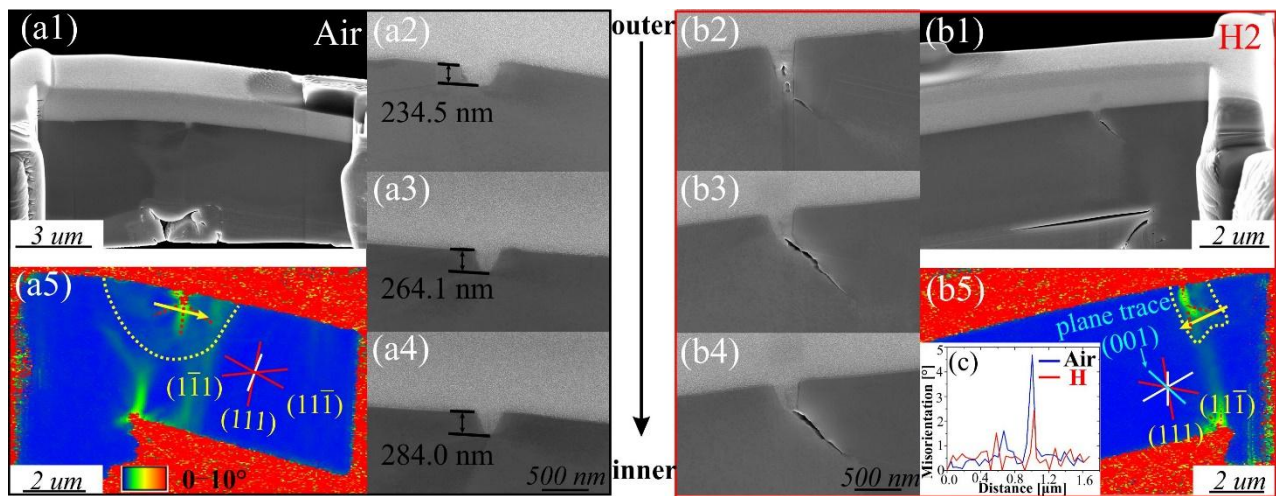

Fig. 3 SE images of beams cross-sections showing details of the cracking behavior (a1-a4) in air and (b1-b4) in H2 condition; (a5), (b5) KAM maps of two beams obtained from t-EBSD; and (c) misorientation data obtained close to the notch cracking.
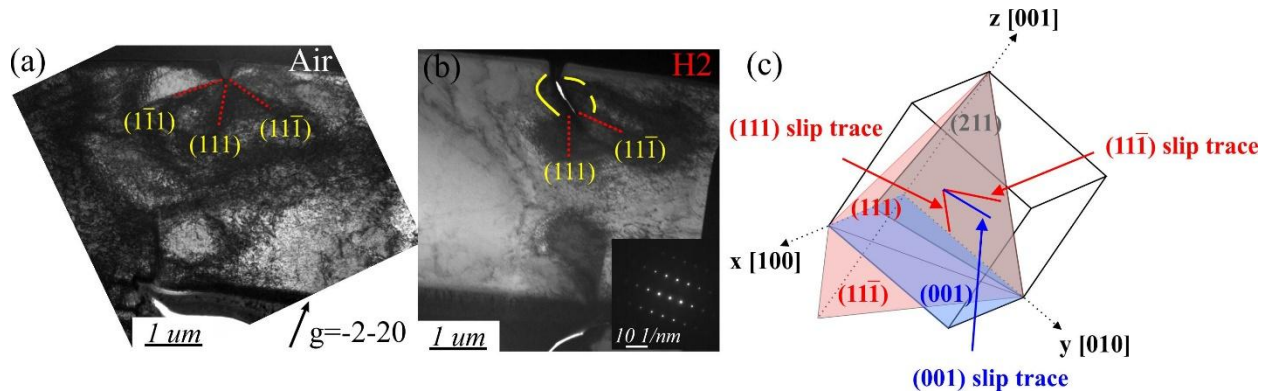
Fig. 4 Bright-field TEM micrographs showing dislocation morphologies of cantilevers bent in (a) air and (b) H2 condition; (c) a schematic showing the relation between the activated {111} slip planes and the (001) crack plane.

Based on the above results, the cracking behavior of the interstitial HEA is highly ~~influence~~ influenced by introducing hydrogen. In the hydrogen-free condition, when the plastic deformation began, the notch tip acted as a stress concentrator and dislocation nucleation started on the slip planes that reached the critical resolved shear stress. Dislocations generated at the notch tip continuously move away, which relieved the local stress effectively and the deformation process continued by notch blunting. All slip systems with the same Schmid factor were activated in the hydrogen-free beam to compensate the deformation process. As a result, a large plastic zone with a value of about 6.28 μm^2 was observed. In contrast, when hydrogen was ~~present~~ presented at the notch tip, we observed a sharp crack with a reduced plastic zone (about 2.83 μm^2) instead of notch blunting. According to the "Defactant" model proposed by Kirchheim [26, 27], the formation energy ~~for~~ of dislocations [24, 28] and vacancies was reduced by adding hydrogen. Dislocation nucleation and multiplication started upon plastic deformation. With hydrogen absorbed into the material and segregated to the dislocations, massive dislocation-dislocation and dislocation-hydrogen interactions were triggered at the notch tip. Also, the creation of strain-induced vacancies was enhanced by hydrogen atoms [29]. Hydrogen and hydrogen-vacancy clusters were proposed to effectively pin dislocations from movement [17, 19, 20, 30], as reflected by the reduced plastic zone at both sides of the crack. With further deformation, dislocations were unable to move away and local strain increased drastically due to pronounced dislocation interactions near the notch front. The local stress intensity gradually reached to the critical value for micro-cracks formation. As a result, the first micro-crack initiated, and the local deformation energy was released. The crack propagation was realized by operating multiple slips on alternating (11$\bar{1}$) and (111) planes, and a mode I crack on (001) plane was created bisecting two {111} planes. In this way, the plastic deformation was continuously consumed by the cracking process. Also, the nucleation and growth of microvoids at slip-band interactions or other defects ahead of the crack tip further ~~contributes~~ contribute to the crack growth and ~~results~~ result in a small crack-tip opening angle [31]. A schematic summary is shown in Fig. 4 (c), where cracking happened along $< 110 >$ direction on (001) plane. The projection of slip planes and crack plane on the beam cross-section is highlighted. The comparable resolved shear stress values for two intersecting conjugate {111} planes ~~was~~ were proposed to cause the decohesion bisecting

slip planes [32]. However, due to the complex stress state and dislocation activities at the notch tip, the values of resolved shear stress on each active slip plane cannot be obtained in the current study. Therefore, further study will be performed by combining elastic-plastic fracture mechanics and discrete dislocation dynamics simulations to analyze the local stress values in each testing conditions.

4. Conclusions

In summary, hydrogen assisted cracking behavior of a carbon-doped equimolar CoCrFeMnNi high-entropy alloy (HEA) was studied by performing the in-situ micro-cantilever bending test in combination with advanced high-resolution characterizing techniques (transmission EBSD and TEM). Pre-notch on {111} plane was chosen as a case study. Results showed that this alloy exhibited superior strength and ductility upon loading in air, notch blunting alone was observed on the bent cantilevers. While in the hydrogen-charged ~~samples~~cantilevers, a sharp cracking on (001) plane bisecting two {111} slip planes was observed. In this study, we show that the initiation and growth of micro-cracks were attributed to the synergetic effect of hydrogen-assisted defects formation and the pinning effect of hydrogen to dislocation motion, which causes the local stress intensity to reach to the critical value for micro-crack formation. As a result, a localized plasticity and a reduced average geometrically necessary dislocation (GND) density were observed. Worthy of mentioning, in order to understand the effect of grain orientation, different crack systems will be designed and tested to get a comprehensive view of hydrogen-assisted cracking in interstitial HEAs.

Data availability

The raw/processed data required to reproduce these findings cannot be shared at this time as the data also forms part of an ongoing study.
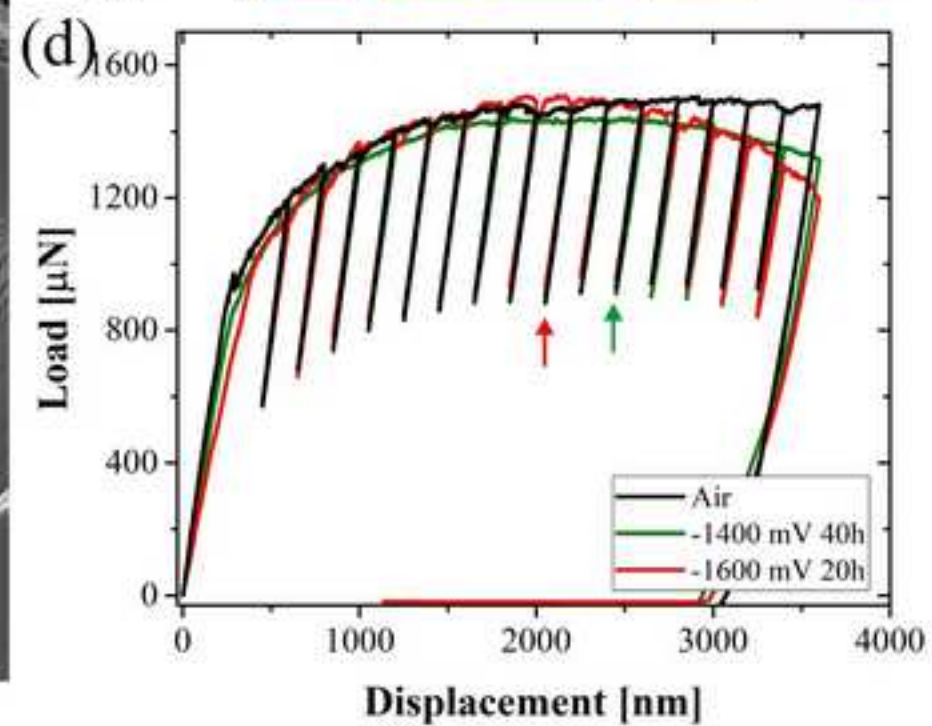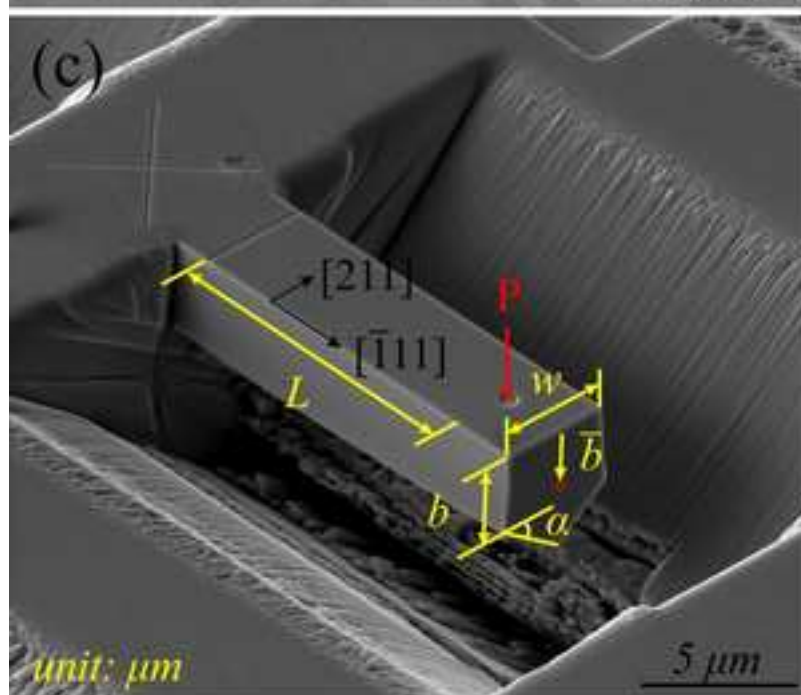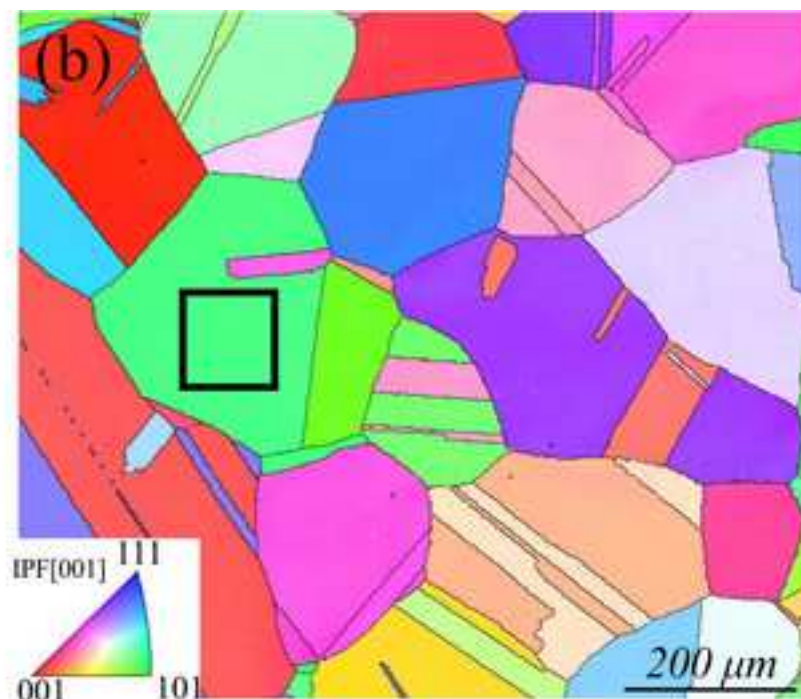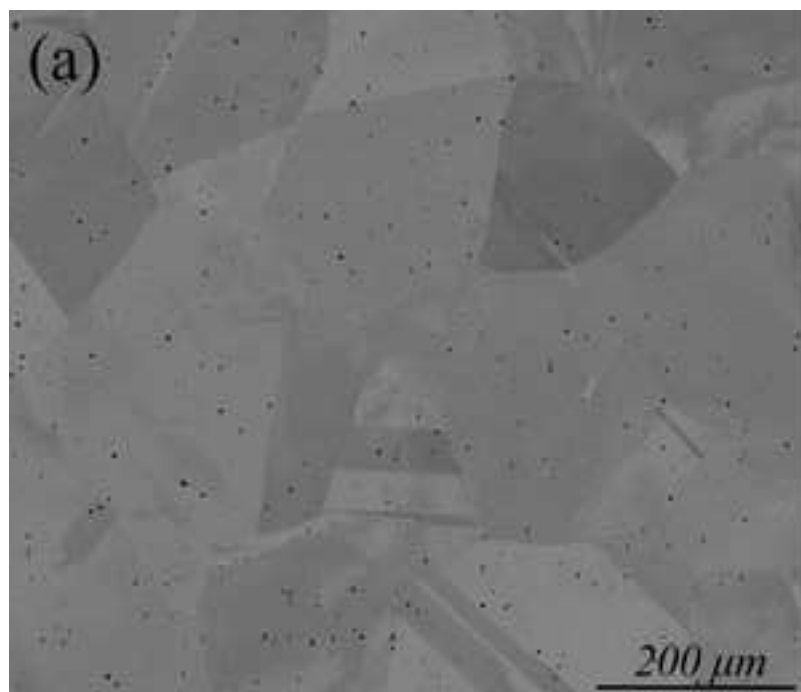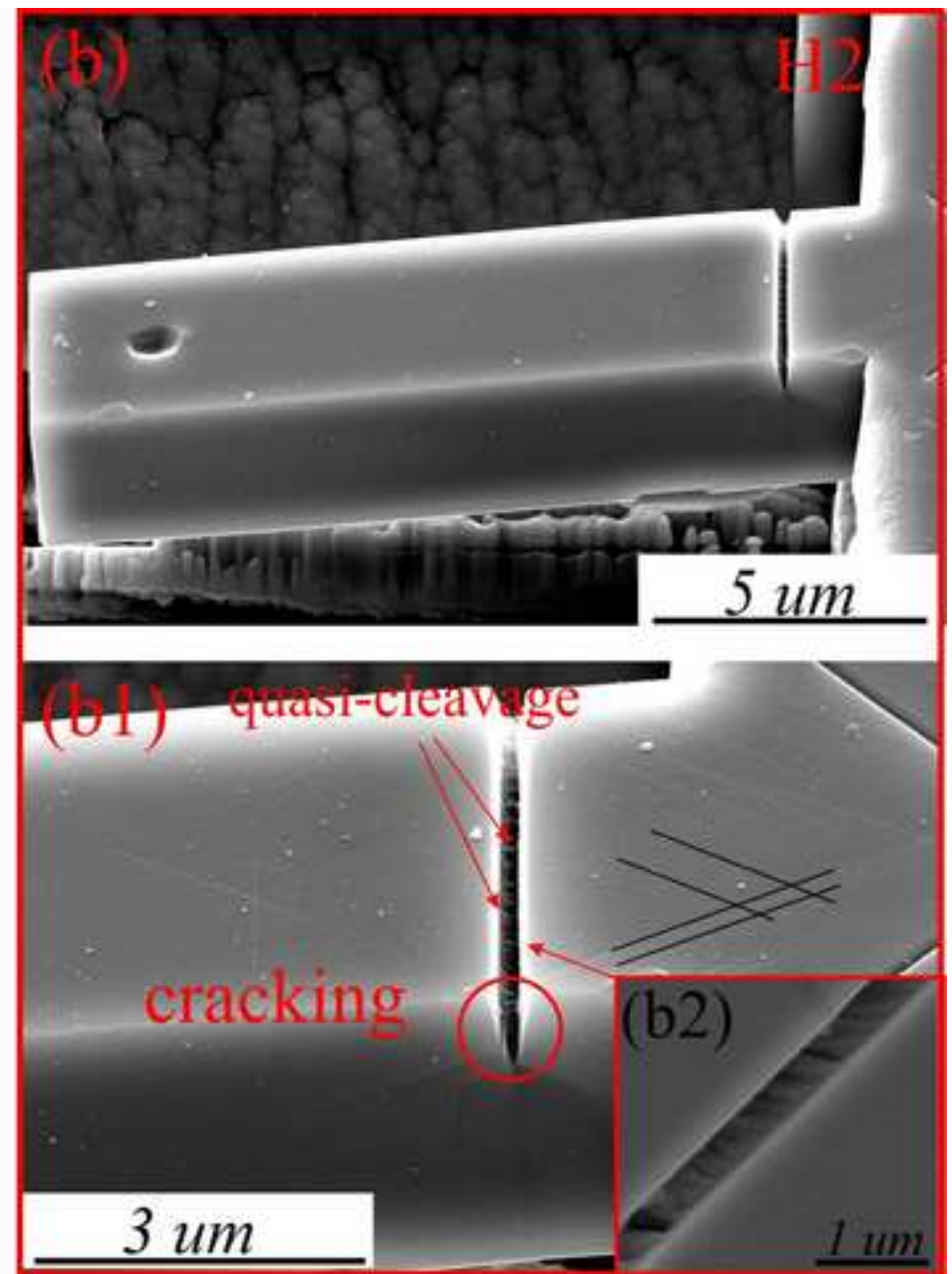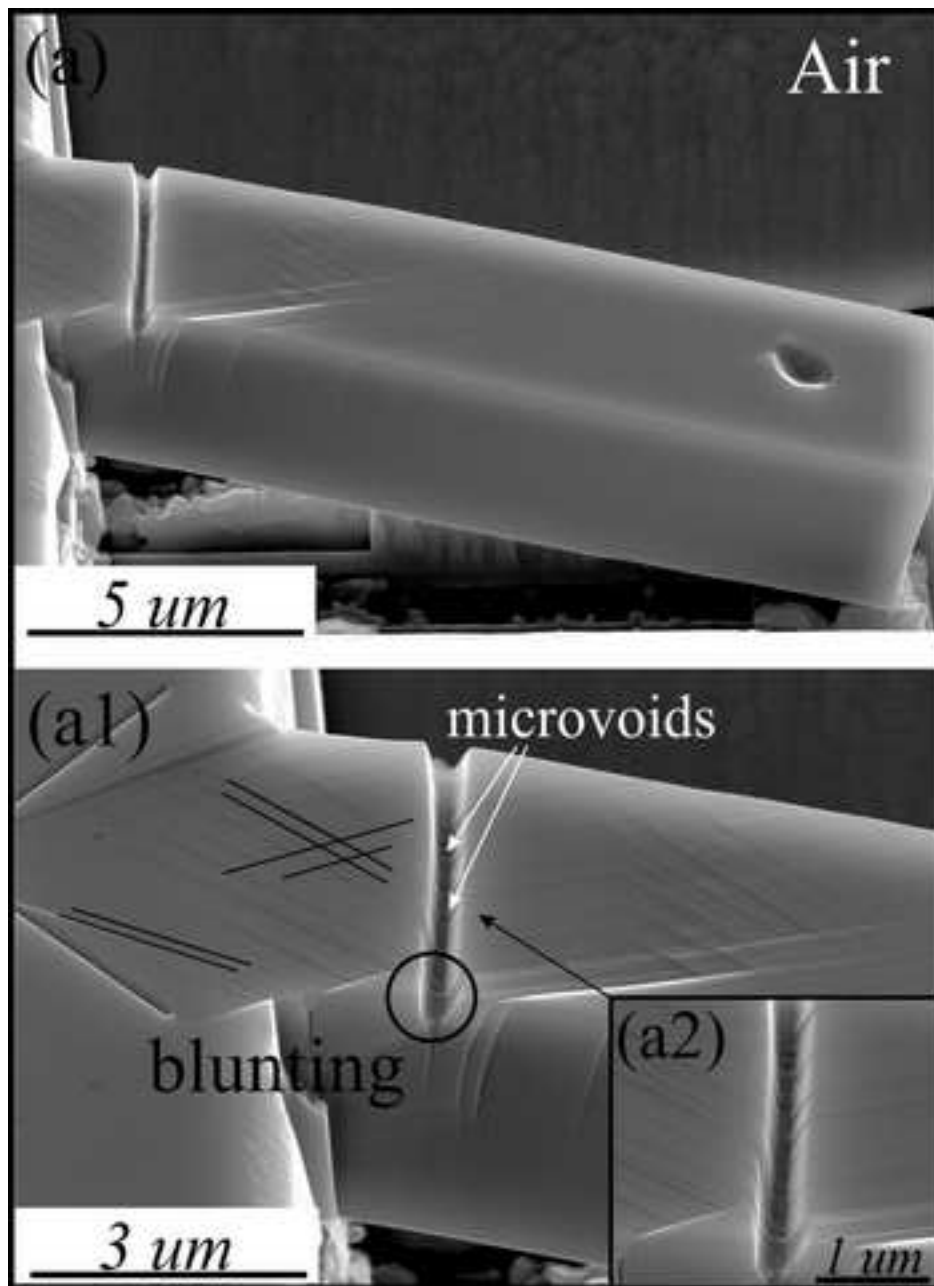
References

[1] J.W. Yeh, S.K. Chen, S.J. Lin, J.Y. Gan, T.S. Chin, T.T. Shun, C.H. Tsau, S.Y. Chang, Nanostructured high-entropy alloys with multiple principal elements: Novel alloy design concepts and outcomes, Adv. Eng. Mater. 6(5) (2004) 299-303.

[2] B. Cantor, I.T.H. Chang, P. Knight, A.J.B. Vincent, Microstructural development in equiatomic multicomponent alloys, Mater. Sci. Eng. A 375 (2004) 213-218.

[3] Z. Li, K.G. Pradeep, Y. Deng, D. Raabe, C.C. Tasan, Metastable high-entropy dual-phase alloys overcome the strength-ductility trade-off, Nature 534 (7606) (2016) 227-30.

[4] Y. Zhang, T.T. Zuo, Z. Tang, M.C. Gao, K.A. Dahmen, P.K. Liaw, Z.P. Lu, Microstructures and properties of high-entropy alloys, Prog. Mater. Sci. 61 (2014) 1-93.

[5] B. Gludovatz, A. Hohenwarter, D. Catoor, E.H. Chang, E.P. George, R.O. Ritchie, A fracture-resistant high-entropy alloy for cryogenic applications, Science 345(6201) (2014) 1153-1158.

[6] F. Otto, A. Dlouhy, C. Somsen, H. Bei, G. Eggeler, E.P. George, The influences of temperature and microstructure on the tensile properties of a CoCrFeMnNi high-entropy alloy, Acta Mater. 61(15) (2013) 5743-5755.

[7] Y.H. Jo, S. Jung, W.M. Choi, S.S. Sohn, H.S. Kim, B.J. Lee, N.J. Kim, S. Lee, Cryogenic strength improvement by utilizing room-temperature deformation twinning in a partially recrystallized VCrMnFeCoNi high-entropy alloy, Nat. Commun. 8 (2017).

[8] A.J. Zaddach, R.O. Scattergood, C.C. Koch, Tensile properties of low-stacking fault energy high-entropy alloys, Mater. Sci. Eng. A 636 (2015) 373-378.

[9] Y.F. Ye, Q. Wang, J. Lu, C.T. Liu, Y. Yang, High-entropy alloy: challenges and prospects, Mater. Today 19(6) (2016) 349-362.

[10] H. Luo, Z. Li, D. Raabe, Hydrogen enhances strength and ductility of an equiatomic high-entropy alloy, Sci. Rep. 7(1) (2017) 9892.

[11] Y. Zhao, D.-H. Lee, M.-Y. Seok, J.-A. Lee, M.P. Phaniraj, J.-Y. Suh, H.-Y. Ha, J.-Y. Kim, U. Ramamurty, J.-i. Jang, Resistance of CoCrFeMnNi high-entropy alloy to gaseous hydrogen embrittlement, Scr. Mater. 135 (2017) 54-58.

[12] H. Luo, Z.M. Li, A.M. Mingers, D. Raabe, Corrosion behavior of an equiatomic CoCrFeMnNi high-entropy alloy compared with 304 stainless steel in sulfuric acid solution, Corros. Sci. 134 (2018) 131-139.

[13] H. Luo, W. Lu, X. Fang, D. Ponge, Z. Li, D. Raabe, Beating hydrogen with its own weapon: Nano-twin gradients enhance embrittlement resistance of a high-entropy alloy, Mater. Today (2018).

[14] K.E. Nygren, K.M. Bertsch, S. Wang, H. Bei, A. Nagao, I.M. Robertson, Hydrogen embrittlement in compositionally complex FeNiCoCrMn FCC solid solution alloy, Curr.Opin. Solid St. M. (2017).

[15] K. Ichii, M. Koyama, C.C. Tasan, K. Tsuzaki, Comparative study of hydrogen embrittlement in stable and metastable high-entropy alloys, Scr. Mater. 150 (2018) 74-77.

[16] H. Luo, Z.M. Li, W.J. Lu, D. Ponge, D. Raabe, Hydrogen embrittlement of an interstitial equimolar high-entropy alloy, Corros. Sci. 136 (2018) 403-408.

[17] Y. Deng, A. Barnoush, Hydrogen embrittlement revealed via novel in situ fracture experiments using notched micro-cantilever specimens, Acta Mater. 142 (2018) 236-247.

[18] T. Hajilou, Y. Deng, B.R. Rogne, N. Kheradmand, A. Barnoush, In situ electrochemical microcantilever bending test: A new insight into hydrogen enhanced cracking, Scr. Mater. 132 (2017) 17-21.

[19] B.R.S. Rogne, N. Kheradmand, Y. Deng, A. Barnoush, In situ micromechanical testing in environmental scanning electron microscope: A new insight into hydrogen-assisted cracking, Acta Mater. 144 (2018) 257-268.

[20] Y. Deng, T. Hajilou, D. Wan, N. Kheradmand, A. Barnoush, In-situ micro-cantilever bending test in environmental scanning electron microscope: Real time observation of hydrogen enhanced cracking, Scr. Mater. 127 (2017) 19-23.

[21] Y. Deng, T. Hajilou, A. Barnoush, Hydrogen-enhanced cracking revealed by in situ micro-cantilever bending test inside environmental scanning electron microscope, Philos. Trans. Royal Soc. A 375(2098) (2017).

[22] Z. Li, Interstitial equiatomic CoCrFeMnNi high-entropy alloys: carbon content, microstructure, and compositional homogeneity effects on deformation behavior, Acta Mater. 164 (2019) 400-412.

[23] A. Barnoush, H. Vehoff, Electrochemical nanoindentation: A new approach to probe hydrogen/deformation interaction, Scr. Mater. 55(2) (2006) 195-198.

[24] D. Wang, X. Lu, Y. Deng, X. Guo, A. Barnoush, Effect of hydrogen on nanomechanical properties in Fe-22Mn-0.6C TWIP steel revealed by in-situ electrochemical nanoindentation, Acta Mater. 166 (2019) 618-629.

[25] B. Bhushan, Springer Handbook of Nanotechnology, 3 ed., Springer-Verlag Berlin Heidelberg2010.

[26] A. Pundt, R. Kirchheim, Hydrogen in metals: Microstructural aspects, Annu. Rev. Mater. Res. 36 (2006) 555-608.

[27] R. Kirchheim, Reducing grain boundary, dislocation line and vacancy formation energies by solute segregation. I. Theoretical background, Acta Mater. 55(15) (2007) 5129-5138.

[28] A. Barnoush, H. Vehoff, Recent developments in the study of hydrogen embrittlement: Hydrogen effect on dislocation nucleation, Acta Mater. 58(16) (2010) 5274-5285.

[29] K. Takai, H. Shoda, H. Suzuki, M. Nagumo, Lattice defects dominating hydrogen-related failure of metals, Acta Mater. 56(18) (2008) 5158-5167.

[30] D. Xie, S. Li, M. Li, Z. Wang, P. Gumbsch, J. Sun, E. Ma, J. Li, Z. Shan, Hydrogenated vacancies lock dislocations in aluminium, Nat. Commun. 7 (2016) 13341.

[31] S.P. Lynch, Mechanisms and Kinetics of Environmentally Assisted Cracking: Current Status, Issues, and Suggestions for Further Work, Metall. Mater. Trans. A 44a(3) (2013) 1209-1229.

[32] Q. Chen, H.W. Liu, Shear fatigue crack growth in large grain polycrystals, Proc. Am. Soc. Test. Mater. 1220 (1995) 467-483.